Journal of Safety Science and Resilience 000 (2022) 1–14

Science Press

Contents lists available at ScienceDirect

Journal of Safety Science and Resilience

journal homepage: http://www.keaipublishing.com/en/journals/journal-of-safety-science-and-resilience/


# Seismic fragility assessment of load-bearing soft-brick unreinforced masonry piers

Jayaprakash Vemuri [a,*], Tariq Anwar [b], KVL Subramaniam [c]

[a] Department Of Civil Engineering, École Centrale School of Engineering, Mahindra University, Telangana 500043, India
[b] Department of Earth Science and Engineering (ErSE), King Abdullah University of Science and Technology, Thuwal, 23955-6900, Saudi Arabia
[c] Department of Civil Engineering, Indian Institute of Technology Hyderabad, Telangana 502285, India

ARTICLE INFO

*Keywords:*
Unreinforced masonry
Soft brick
Micro-modeling
Nonlinear time history analyses
Synthetic ground motions
Seismic fragility

ABSTRACT

Unreinforced masonry (URM) made with soft bricks comprises a large percentage of the building stock in developing countries. However, the poor performance of URM piers during earthquakes has led to renewed interest in understanding their behavior under lateral loads. Little experimental data is available on the seismic response, analysis, and design of URMs made of soft bricks. In this study, the micro-modeling technique is used to simulate the in-plane behavior of load-bearing, soft-brick URM piers. The parameters required in the constitutive models are obtained from material tests and used to develop a calibrated numerical model of the URM piers. Piers with various aspect ratios subjected to various axial stresses are numerically modeled to obtain monotonic and cyclic responses, and their critical displacement limit states are identified. Changes in the failure modes of masonry piers with variations in the aspect ratio and axial stress are established. Load-bearing piers exhibit three distinct failure modes: bed sliding, diagonal shear cracking, and flexure, depending on the aspect ratio and axial stress. The seismic fragility of each pier failure type is examined using nonlinear time history analyses. The results show that bed-sliding piers collapse at extremely low PGA levels. Piers failing through diagonal shear cracking also fail at low PGA levels. Flexural piers can resist seismic forces up to a slightly higher PGA level and thus are the last to collapse. The results also indicate that the effect of uncertainty in ground motions is more significant than the effect of variability in the masonry pier capacities.

## 1. Introduction

A large percentage of the building stock on the Asian sub-continent comprises brick masonry, unreinforced adobe, and block masonry construction; In India, such construction accounts for 69% of the total building stock [1]. In contrast to reinforced brick masonry, which has steel reinforcing bars placed in either the vertical or horizontal direction and often in the joints to enhance the tensile behavior, unreinforced masonry (URM) structures have load-bearing URM piers that are primarily designed to support only gravity loads [2]. Damage reconnaissance surveys after earthquakes in Kashmir (2005), Gujarat (2001), and Nepal (2015) indicated extensive damage to load-bearing URM structures. Often, the failures reported in earthquakes are obfuscated by issues of construction quality and other problems related to the non-engineered nature of these structures. Performing scenario-specific evaluation is complicated by the lack of proper models for the cyclic response of URM used in these regions. Most of the existing experimental data and calibrated numerical models for the hysteretic behavior of masonry were developed for URM built with stiff bricks, where the mortar has a lower stiffness than the brick units. In the Indian sub-continent, steady improvements in the quality of cement have resulted in mortars that have higher stiffness and compressive strength than bricks [3]. Outdated production processes for the manufacture of bricks, still in practice in India, result in large-scale production of soft bricks with low stiffness [4]. Typically, mortar has a stiffness comparable to or higher than that of brick [5,6]. Calibrated models for soft-brick masonry are not available in the literature; however, such models are required to perform scenario-specific damage evaluations. The complex interaction of the two constituents of URM, i.e., brick and mortar, influences the structural response. Several studies [7–10] have evaluated the behavior of masonry made with stiff bricks. The cyclic behavior of stiff-brick URM piers has been observed by performing pseudo-dynamic experiments [11–15], leading to recommendations for lateral drift capacities for various modes of failure.

However, the load response of soft-brick URM piers has not been adequately evaluated, either experimentally or numerically. Recently, the compressive behavior of soft-brick masonry was examined experimentally [3,16]; it was concluded that failure was affected by the tensile strength of the mortar. The compressive failure of soft-brick prisms with high-strength mortar was found to be caused by localized crush-

* Corresponding author.
*E-mail address:* jayaprakash.vemuri@mahindrauniversity.edu.in (J. Vemuri).

https://doi.org/10.1016/j.jnlssr.2022.05.001
Received 9 April 2022; Received in revised form 16 May 2022; Accepted 19 May 2022
Available online xxx

ing, which resulted in global instability under applied compression. For mortar with a lower strength than that of the brick unit, failure is associated with spalling produced by multiple cracks. The cohesive-frictional shear response of the brick mortar interface has also recently been investigated experimentally [16,17] for low to moderate confining stresses. It was observed that the shear stress transfer between the brick and mortar in masonry is limited by cracking at the interface. A material model was developed for the shear stress transfer between bricks bonded with mortar in soft-brick masonry under applied compression [18].

Typical soft-brick URM buildings are composed of several load-bearing masonry piers with various aspect ratios arranged in orthogonal planes. The stability of the structure is governed primarily by the in-plane action of the URM piers [11]. Determining the in-plane seismic fragility of various types of URM piers can aid in understanding the vulnerabilities of URM buildings. In recent years, seismic fragility analysis has emerged as a useful tool for earthquake risk assessment because it presents a framework that combines uncertainties based on both the seismic demand and structural capacity [19–23]. Seismic fragility is the probability that a system response will exceed a critical level under seismic loading of specified intensities. While the critical level is represented by the damage limit states for the system, the seismic intensity may be represented by any parameter representing ground shaking. In essence, seismic fragility is the conditional probability of exceeding a damage limit state for a specific level of seismic intensity. The limit-state probabilities of exceeding the structural response parameter are derived as shown in Eq. (1). This procedure enables comprehensive fragility assessment of various structure-specific/identified limit states.

$$Fragility = P[Demand > Capacity | Ground\ Motion\ Intensity] \tag{1}$$

Seismic fragility assessments using nonlinear time history analyses require a suite of strong ground motions. Furthermore, in a scenario-specific evaluation, the ground motions used in the analyses must be representative of the intensity, frequency content, and duration expected at the site of interest [24]. This represents a challenge, particularly in the absence of a historical database of recorded ground motions in many regions. To address this issue, source-based stochastic simulations can be performed to generate synthetic ground motions [25–27]. This approach accounts for both the fault rupture characteristics and explicitly considers the seismic wave propagation to the site, i.e., the path and site effects. Finally, to obtain accurate surface-level synthetic ground motions, site amplification functions for each site must be used.

This study assesses the seismic vulnerability of soft-brick URM piers using a scenario-based analytical fragility approach. A scenario-based analytical fragility assessment method is used to evaluate the performance of URM piers subjected to ground motions from a defined earthquake scenario. This method has been used to estimate the seismic demand due to maximum considered earthquakes [28,29]. In this study, to perform the seismic fragility analyses, a suite of soft-brick URM pier models is assembled by considering various material and geometric properties of the piers. Finite element analyses of these piers are performed using a micro-modeling approach. The critical displacement limit states of various soft-brick piers are identified using stress-based criteria. Nonlinear time-history analyses of the complete suite of URM piers are performed using synthetic ground motions obtained for the Mw 7.6 2001 Gujarat earthquake scenario. The displacement responses of the various soft-brick URM piers are analyzed and compared with the critical displacement limit states. Finally, the URM pier performance is measured and fragility curves are developed. The vulnerabilities of specific failure modes of the masonry are identified.

## 2. Numerical modeling of soft-brick URM piers

A micro-modeling approach was used to develop a representation of the masonry. In this approach, the repetitive pattern of the brick units is represented using continuum elements. The interactions between individual brick elements are represented using interface elements. The interface elements provide the normal and shear stress transfer between individual brick elements. Using the micro-modeling approach, a detailed analysis of the influences of the brick unit, mortar, and brick–mortar interface on the lateral load response of a masonry panel can be evaluated [30–34]. In the micro-modeling approach, all of the nonlinearity in the mortar and brick–mortar interface is lumped at the interface. This reduces the computational effort compared to the detailed micro-modeling approach, in which the detailed model of the mortar and brick requires a large number of elements. The element size in the detailed model is determined by the thickness of the mortar, which makes the analysis very computationally expensive. The macro approach, which is conventionally used to analyze the behavior of masonry, uses a smeared representation of the brick, mortar, and brick–mortar interface [35]. This approach does not allow for prediction of the interactions between different elements or for geometric representation of repetitive elements within the masonry. The micro-modeling technique for predicting the load response of URM under a combination of loads requires the properties of the interface elements, which can be derived from material tests [3,17,18].

Fig. 1(a) shows the actual masonry sample with brick units and bed and head joints. Fig. 1(b) shows the micro-modeling approach, where the failures are focused at the joint interfaces. Tensile crack interfaces are located vertically in the middle of the units to allow cracking within the brick elements. Zero-thickness interface elements are used to represent the mortar head and bed joints. The units are expanded by a half-thickness of the mortar in both directions.

Using the generalized strain and stress vectors, the interface model is represented as

$$\sigma = D \cdot \varepsilon, \tag{2}$$

where

$$\sigma = [\sigma \quad \tau]^{\mathrm{T}}, \tag{3}$$

$$\varepsilon = \left[\Delta u_n \quad \Delta u_t\right]^{\mathrm{T}}, \tag{4}$$

$$D = diag\left[k_n \quad k_t\right], \tag{5}$$

in which $\sigma$ and $\Delta u_n$ are the normal stress and relative displacement, respectively; $\tau$ and $\Delta u_t$ are the shear stress and relative displacement, respectively; and $k_n$ and $k_t$ are the normal and tangential stiffness, respectively.

The normal and shear stiffnesses, $k_n$ and $k_t$, respectively, of the interface elements are also derived for soft-brick masonry. The total lateral displacement for the applied shear stress, $\tau$ (Fig. 2(a)), is given by the following:

$$u_t = \frac{\tau}{G_b} \cdot \left(\frac{h_b}{2}\right) + \frac{\tau}{G_m} \cdot h_m + \frac{\tau}{G_b} \cdot \left(\frac{h_b}{2}\right) + 2 \cdot \frac{\tau}{G_{int}}. \tag{6}$$

The total lateral displacement for the equivalent micro-model (Fig. 2(b)) is given as

$$u_t = \frac{\tau}{G_b} \cdot (h_b + h_m) + \frac{\tau}{G_{int}}. \tag{7}$$

By equating Eqs. (6) and (7), the shear modulus of the interface can be obtained as follows:

$$G_{int} = k_t = \frac{1}{h_m}\left[\frac{G_b G_m}{G_m - G_b}\right]. \tag{8}$$

Using a similar procedure, the normal stiffness of the interface is obtained as

$$E_{int} = k_n = \frac{1}{h_m}\left[\frac{E_b E_m}{E_m - E_b}\right], \tag{9}$$

where $G_m$ is the shear modulus of the mortar joint, $G_b$ is the shear modulus of the brick, $G_{int}$ is the shear modulus of the brick–mortar interface, $E_m$ is the elastic modulus of the mortar joint, $E_b$ is the elastic modulus

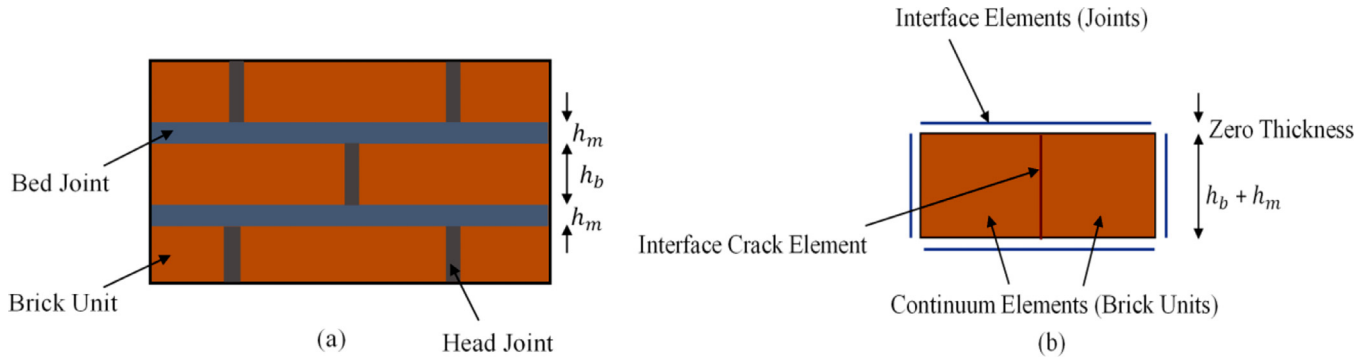


**Fig. 1.** (a) Actual masonry sample; (b) micro-modeling approach.

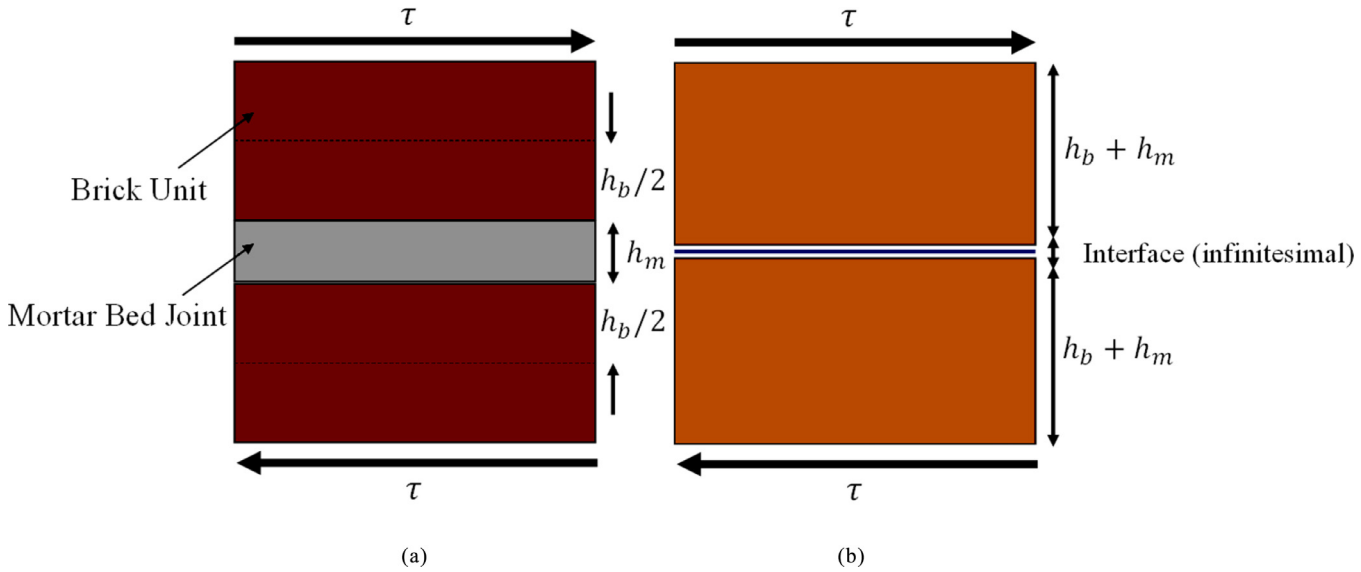


**Fig. 2.** (a) Masonry brick and joint sample; (b) equivalent micro-model.

of the brick, $E_{int}$ is the elastic modulus of the brick–mortar interface, $h_b$ is the height of the brick unit, and $h_m$ is the height of the mortar joint.

The finite element model was developed using the specialized interface and continuum elements available in DIANA$^{TM}$ [36]. In the finite element model of the masonry, each brick unit was modeled using two plane stress, 8-noded continuum elements. Tensile fracture in the brick was considered by introducing interface fracture elements between the continuum elements. The material properties of the interface crack and interface elements were obtained from material test results. The vertical interface between the continuum elements within a brick unit was represented using interface elements with large normal and shear stiffnesses to prevent interpenetration [37,38]. In tension, a bilinear tensile stress crack separation relationship with a linear tangent stiffness followed by a linear decrease in the post-peak tensile stress was assumed. The tensile strength, $f_t$, of the vertical interface between brick units was taken as 1/10 the brick strength [39]. The tensile fracture energy and tensile strength of the brick were obtained from an interpolation plot between the fracture energy and tensile strength of the brick [39].

Interface elements were used for the head and bed joints of the masonry. For the interface elements, the normal stiffness, $k_n$, and tangential stiffness, $k_t$, were calculated using Eqs. (8) and (9), respectively. The values of the other material constants were obtained from compression and direct shear tests on triplet masonry specimens using bricks with a Young's modulus of 0.7 GPa and a compressive strength of 14 MPa [17,18]. The Young's modulus of the brick was found to be 50 times its compressive strength, which was also observed in the other test data. The Poisson's ratio of the brick unit was found to be consistently equal to 0.25. The interface shear behavior of the brick–mortar interface was investigated using mortars with compressive strengths varying between 5.8 and 30 MPa [3,17]. The Young's moduli of the mortars ranged between 8 and 27 GPa. From the test data, it was found that the Young's modulus of the mortar could be estimated as 1000 times its compressive strength. The Poisson's ratio of the mortar was found to be consistently equal to 0.2, irrespective of the mortar strength. The interface joint test data derived from bricks that were of low stiffness compared to the mortar were found to vary with the mortar strength [17,18]. Table 1 summarizes the material properties of the interface elements and joints derived for mortar and brick compressive strengths of 5.8 and 14 MPa, respectively.

### 2.1. Validation of the numerical approach

A full-scale soft-brick URM pier was experimentally tested [16] under lateral displacement with applied compression. The compressive strengths of the brick and mortar were 21.2 and 6.6 MPa, respectively. The pier had a height of 3 m, length of 3 m, and thickness of 0.24 m. The brick units had dimensions of 240 mm × 100 mm × 75 mm. The pre-compression vertical load applied on the pier was computed assuming a single-story building with dimensions of 3 m × 3 m × 3 m comprising a reinforced concrete slab with a thickness of 0.1 m and a masonry parapet pier with a height of 1 m above the concrete slab. These properties were used to validate the numerical approach. The authors reported the initiation of flexural cracking at 2 mm, which propagated further with

**Table 1**
Material parameters of the interface material model.

| Materials | Material Properties | Value |
|---|---|---|
| **Bricks** | Young's modulus, $E$ (N/mm$^2$) | 50 × brick strength |
| | Poisson's ratio, $\nu$ | 0.25 |
| **Interface** | Linear normal stiffness, $k_n$ (N/mm$^3$) | 1,000,000 |
| **Crack** | Linear tangential stiffness, $k_t$ (N/mm$^3$) | 1,000,000 |
| | Tensile strength, $f_t$ (N/mm$^2$) | 1/10 (comp. str.) |
| | Tension softening fracture energy (N/mm) | 0.08 |
| **Joints** | *Structural Parameters* | |
| | Cohesion, $c$ (N/mm$^2$) | 0.14 |
| | Friction angle, $\mu$ (rad) | 0.65 |
| | Dilatancy angle, $\psi$ (rad) | 0.001 |
| | Residual friction coefficient (rad) | 0.58 |
| | Confining normal stress for $\Psi_0$ dilatancy (N/mm$^2$) | −1.3 |
| | Exponential degradation coefficient (softening parameter) | 5 |
| | *Mode I Parameters* | |
| | Tensile strength, $f_t$ (N/mm$^2$) | 0.1 |
| | Fracture energy, $G_f^I$ (N/mm) | 0.001 |
| | *Mode II Parameters* | |
| | Factor (a) | 0 |
| | Factor (b), $G_f^{II}$ | 0.125 |
| | *Compression Cap Parameters* | |
| | Cap critical compressive strength, $f_c$ (N/mm$^2$) | 5.8 |
| | Shear traction control factor, $C_s$ | 9 |
| | Compressive fracture energy, $G_{fc}$ (N/mm) | 5 |
| | Equivalent plastic relative displacement, $k_p$ | 0.093 |

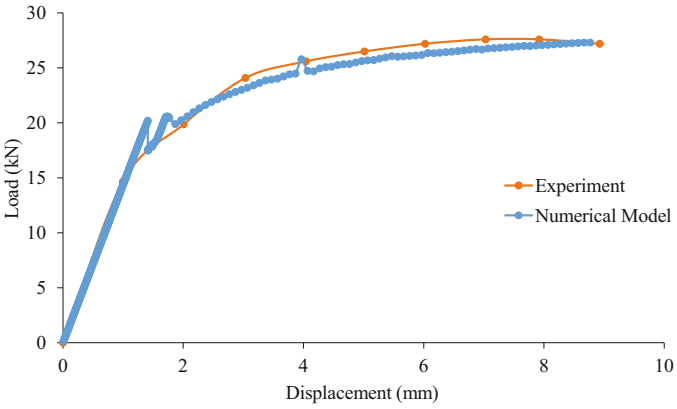


**Fig. 3.** . Comparison of experimental and numerical monotonic responses.

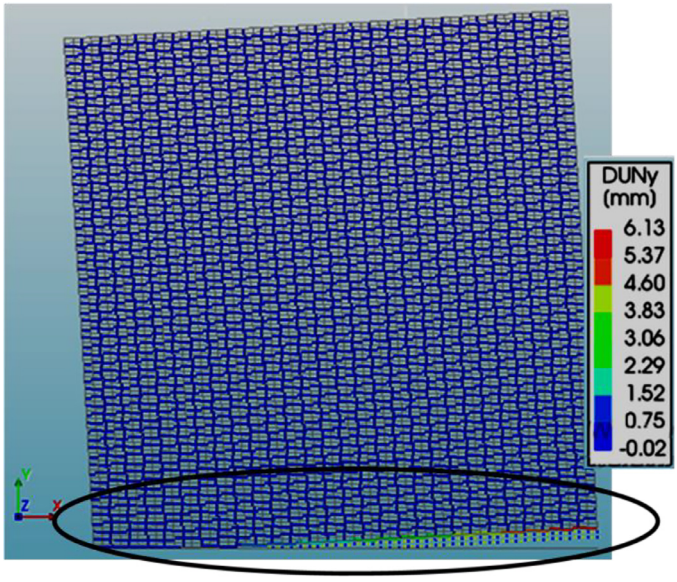


**Fig. 4.** Displacement crack pattern of the pier at failure.

an increase in displacement, leading to a final failure through sliding shear.

The properties of the interface crack and joint were derived using Eqs. (8) and (9). Numerical modeling of the masonry piers was performed using finite element analysis software. The numerical analysis consisted of two steps: in the first step, vertical gravity loads were applied; in the second step, incremental displacement in the horizontal direction was applied. The conventional Newton–Raphson method was used to solve the nonlinear equations at each step of the analysis. The convergence at each step was checked using an energy criterion with a tolerance of 0.001 N·mm. Fig. 3 shows that a good match was obtained between the experimental and numerical results. Fig. 4 shows the observed displacement crack pattern in the numerical model, which was similar to the observed tensile cracking and sliding failure reported in the experiment [16].

### 2.2. Monotonic responses of soft-brick URM piers

The micro-modeling approach was used to develop the numerical model in DIANA. Fig. 5 shows the details of a pier and a representation of the mesh adopted for the pier. Aspect ratios of 0.5, 0.75, 1, and 1.5 were chosen to model the piers. All of the piers were 3.0 m in height, and the width of the piers was varied to explore the influence of the aspect ratio on the failure mode of soft-brick URM piers. Studies performed on stiff-brick masonry have indicated that the aspect ratio of the piers influences the lateral load response of URM piers [11]. The compressive strengths of brick, mortar, and masonry were taken as 14 MPa, 7 MPa, and 5.8 MPa, respectively, based on experiments [3]. The dimensions of the brick units were 50 mm (height) × 210 mm (width), and the joint mortar thickness was 10 mm. The Young's modulus and Poisson's ratio of the brick unit were 1000 MPa and 0.25, respectively. The Young's modulus and Poisson's ratio of the mortar were 9720 MPa and 0.21, respectively. Considering the possible levels of gravity loads acting on load-bearing URM piers [4], the URM pier models were subjected to axial stresses of 0.1, 0.5, and 0.75 MPa.

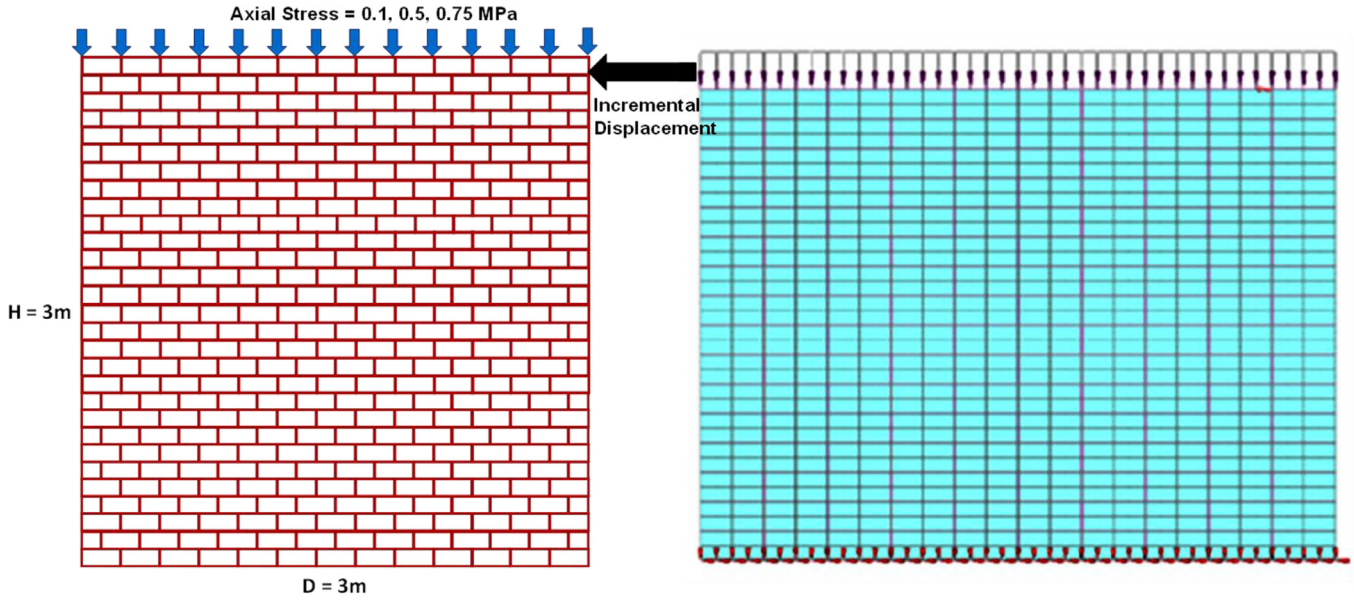


**Fig. 5.** (a) Pier details; (b) pier mesh in DIANA®.

**Table 2**
Failure matrix for soft-brick URM piers.

| Axial Stress/Compressive Strength | Aspect Ratio (H/L) | | | |
|---|---|---|---|---|
| | 0.5 | 0.75 | 1 | 1.5 |
| 0.017 | Sliding | Flexure | Flexure | Flexure |
| 0.086 | Shear | Shear | Flexure | Flexure |
| 0.129 | Shear | Shear | Flexure | Flexure |

Three distinct failure modes were identified in the in-plane responses of the URM piers. The cracking and failure were associated with sliding, diagonal cracking (shear), and flexure (rocking and toe crushing). The various failure modes are summarized in Table 2, depending on the axial stress ($\sigma$) and aspect ratio (H/L) of the pier. It is observed that sliding failure occurs at a low applied axial stress of 0.1 MPa. At low axial stress, with increasing aspect ratio, H/L, the failure mode changes to flexure. With increasing axial stress at a low aspect ratio, H/L (stocky pier), the failure mode changes to diagonal shear cracking. At higher aspect ratios, H/L (slender piers), of 1.0 and 1.5, flexural failure with toe crushing is observed. For piers with an intermediate aspect ratio, H/L, of 0.75, rocking/flexure is the predominant failure mode at low axial stress, while shear failure is observed in piers with higher axial stresses of 0.5 and 0.75 MPa. There are distinct changes in the failure modes with increases in the axial stress level and aspect ratio.

The typical response of a pier with H/L = 0.5 and an axial stress of 0.1 MPa, which exhibits sliding failure, is shown in Fig. 6. Three critical limit states are identified based on the behavior of the sliding pier. There is an onset of flexural cracking at the bottom of the pier at 0.6 mm, followed by the onset of sliding at a displacement of 3 mm. Finally, there is a complete loss of the bond at 4 mm, which is identified as the collapse state. The bed-sliding failure mode occurs under low axial loads and is characterized by tensile cracking in the bed joints, leading to the formation of sliding planes. The resulting movement along the bed joint is accompanied by a decrease in the load due to reduced frictional resistance.

Fig. 7 shows the typical response of a pier with H/L = 0.75 subjected to a compression level of 0.5 MPa. The pier fails in shear and exhibits diagonal stair-step cracking. Three critical limit states are identified based on the behavior of the shear pier. Flexural cracks originate at 2.1 mm. Visible diagonal cracking is observed at 7.3 mm close to the ultimate shear strength, which is followed by a drop in strength at 8 mm. Primarily, shear failure is characterized by diagonal cracking, either through the brick unit or the mortar head joints. In the post-peak regime, the strength decreases rapidly while dissipating energy. Typically, the pier collapses via stepped cracking along the bed and head joints.

Fig. 8 shows the typical response of a pier with an aspect ratio of H/L = 1.5 failing in flexure. There is an onset of flexural cracking at 2.9 mm followed by collapse at 14 mm. Flexural failure is observed either as toe-crushing of units in the toe region of the pier (compression) or by rocking of the pier at the bottom corner (tension). As the horizontal displacement demand increases, the bed joints crack in tension, and the compressed masonry carries the shear. The final failure is observed as an overturning of the pier along with the crushing of the compressed corner.

Fig. 9 shows the typical cyclic hysteresis behavior observed for the sliding, shear, and flexural failure modes. An increasing, fully reversed cyclic loading history consisting of one cycle for each peak displacement was applied. Each failure mode exhibits a different hysteretic response. The hysteretic behavior during sliding failure is shown in Fig. 9(a). A symmetrical response with hysteresis loops following elastic perfectly plastic-type behavior has been reported for a pier that fails through bed-joint sliding [14]. The observed hysteretic behavior agrees with the experimental hysteresis for the *bed-joint sliding failure mode* given in FEMA 307 [40]. A typical hysteretic response under shear failure is shown in Fig. 9(b). The reverse cyclic response exhibits symmetric responses in both loading directions. The envelope exhibits strength degradation with increasing deformation. The unloading behavior under the applied load reversals exhibits stiffness degradation. There is no pinching upon load reversal. The hysteretic load response of piers failing through diagonal cracking has been observed to exhibit pivot-type behavior in experiments [11]. The hysteretic response agrees with the cyclic response of the *shear failure mode* given in FEMA 307 [40]. Fig. 9(c) shows the cyclic hysteresis response of flexure-type failure. The response is symmetrical, and the hysteretic behavior resembles elastic strain-hardening plastic behavior (without the Bauschinger effect). The predicted hysteretic behavior agrees with the experimental cyclic response obtained for piers failing through flexural cracking and toe crushing [13,14]. The hysteresis behavior of the *flexural failure mode* matches the typical response in FEMA 307 [40].

Based on the observed cyclic behavior, the *isotropic* hysteresis model, *multi-linear pivot* model, and *kinematic* models available in SAP2000

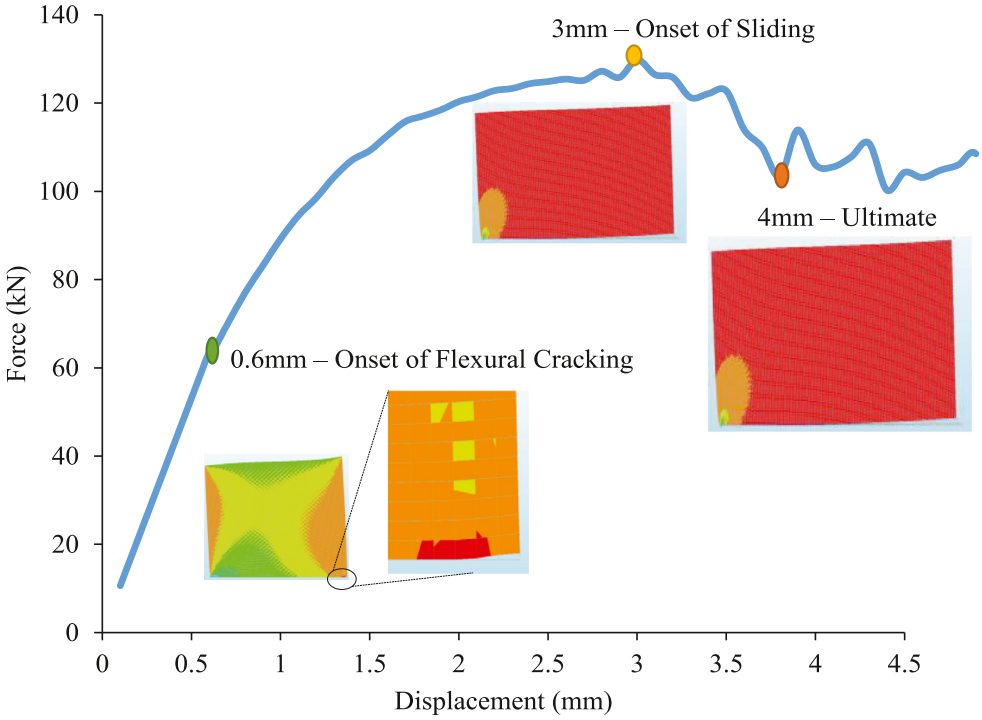


**Fig. 6.** Monotonic response of a soft-brick URM pier failing through bed-sliding.

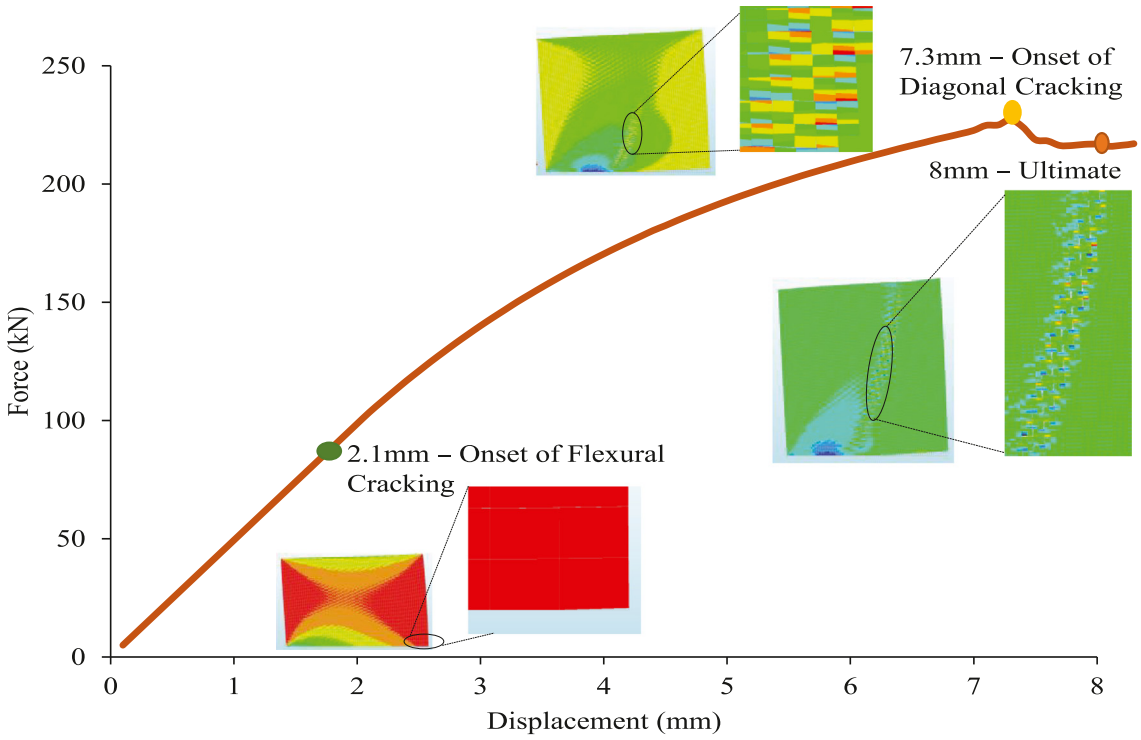


**Fig. 7.** Monotonic response of a soft-brick URM pier failing through diagonal shear cracking.

[41] were adopted for the sliding, shear, and flexural piers, respectively. In all three hysteretic models, the monotonic backbone curve of the respective piers is provided, along with the mass and initial stiffness. For the pier failing in shear, additional pivot parameters for the multi-linear plastic pivot model, which control the hysteresis loop shape, strength, and stiffness degradation, were calibrated based on the simulated cyclic response. The pivot parameters were obtained by minimizing the least-squares error with respect to the simulated response.

## 3. Seismic fragility analysis

Seismic fragility evaluation was performed by combining the uncertainties in the demand and capacity. The structural response, i.e., the *pier displacement*, is a function of the variation in ground motions and URM material properties. The effect of variation in the material properties was investigated using the Latin hypercube sampling technique, and the effect of ground motion uncertainty was incorporated by us-

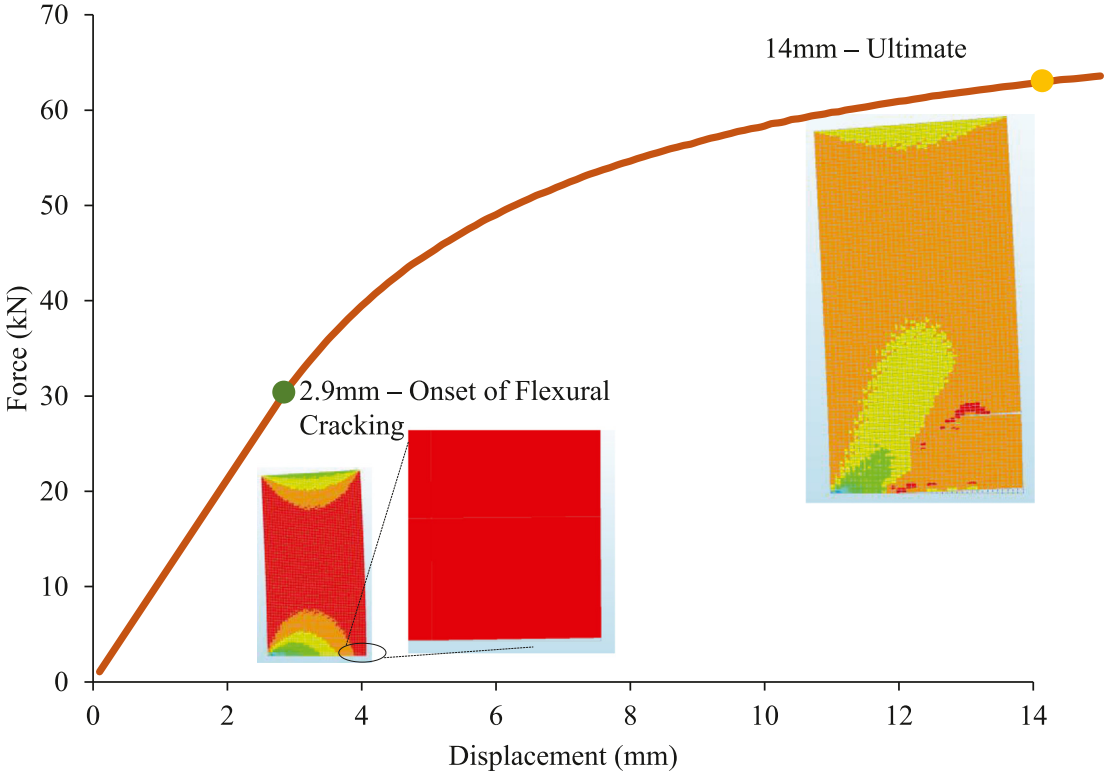


**Fig. 8.** Monotonic response of a soft-brick URM pier collapsing in flexure.

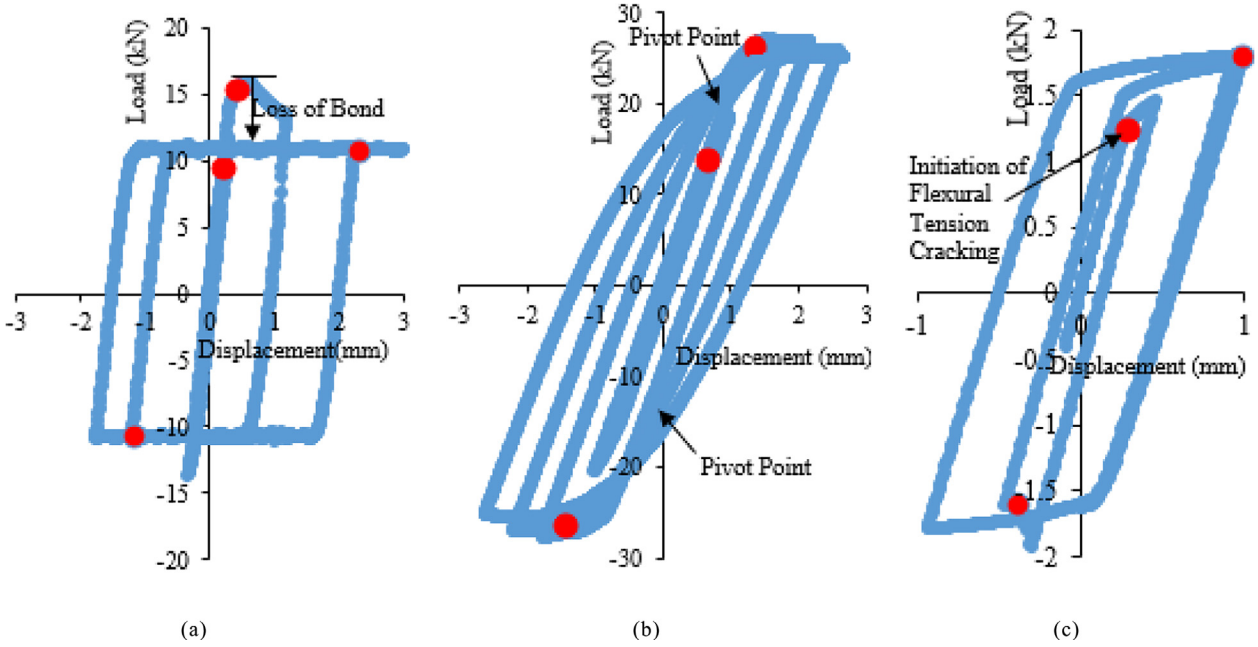


**Fig. 9.** Typical cyclic responses for soft-brick piers exhibiting (a) sliding, (b) shear, and (c) flexural failure.

ing 10 realizations of ground motions at each peak ground acceleration (PGA) level. A ground motion suite consisting of various levels of ground motions for the 2001 Bhuj earthquake was used for the scenario-specific assessments. A suite of ground motions allows for evaluation of the probability that the URM pier will be subjected to individual damage states. The capacity variability was developed by considering various uncertainties in the material and geometric properties of the pier. The suite of URM pier models was subjected to a suite of ground motions, and the structural responses of the URM piers were analyzed. In the present study, the displacement response of soft-brick URM piers was compared with the critical displacement limit states identified in the lateral load responses of the soft-brick URM piers. The collapse fragility curves were obtained based on the probability of exceeding the limit states ($P_f$) for different seismic intensity parameters, such as the PGA and peak ground velocity (PGV). Fig. 10 shows a flowchart illustrating this procedure. It has been observed previously [42] that 10 realizations of the seismic demand (represented by ground motions) and 10 representations of the structural capacity (represented by backbone curves) can be combined

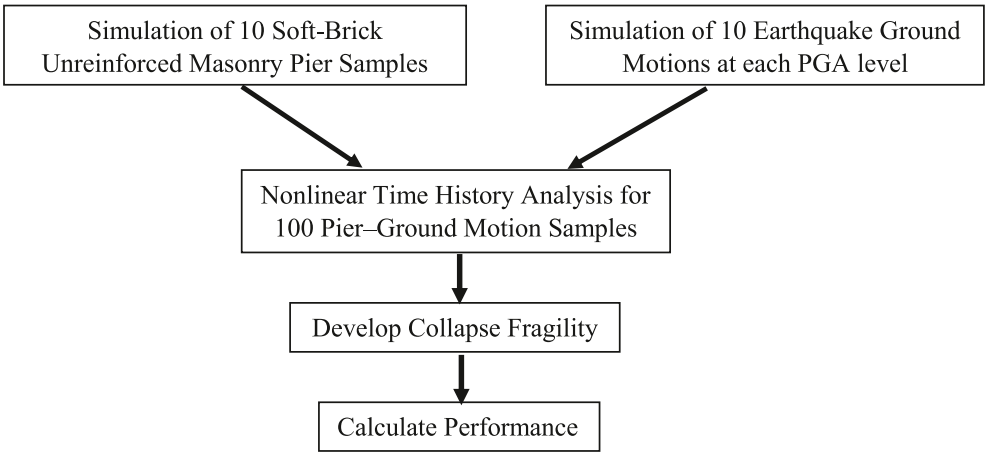


**Fig. 10.** Flowchart illustrating the methodology for the fragility analysis.

to provide an adequate set of 100 pier–ground motion samples to determine the variation in structural response and compute the seismic fragility.

### 3.1. Uncertainty in the capacity of soft-brick URM piers

The effect of uncertainty in the URM pier capacity was identified by performing a sensitivity analysis of the various parameters used in the numerical model. All of material parameters were varied (±20%) to examine their influence on the monotonic pushover curves: those influencing the slope or peak load significantly (greater than 1% variation for a 20% variation in the parameter value) were noted. The capacity curve for the pier failing in shear was observed to be sensitive to three parameters: two properties of the interface (the cohesion and friction angle) and one property of the brick (the Young's modulus). The capacity curve for the pier failing through bed-sliding was observed to be sensitive to five parameters: two properties of the brick (the Young's modulus and Poisson's ratio) and three properties of the interface (the cohesion, friction angle, and residual friction coefficient). The capacity curve for the flexural pier was observed to be sensitive to only one parameter: the Young's modulus of the brick. All of the sensitive parameters were assumed to have a normal distribution with 10% dispersion around the mean. Subsequently, these sensitive parameters were used to perform simulations for various URM piers. However, traditional Monte Carlo simulations require an extremely large number of simulations, and the sampling is completely random, leading to a preference or exclusion of some sample pairs [43]. These two issues were addressed by using the Latin hypercube sampling (LHS) technique [42]. The LHS technique reduces computational effort and ensures that samples are drawn from the entire range of the distribution. The LHS technique essentially divides the probability distribution function into a histogram of equal intervals, thus ensuring that each sample has an equal probability of occurrence. For each variable, samples are generated from each interval of their respective distributions and then randomly combined to obtain a random pairing of samples [44]. In this study, using samples obtained with the LHS technique, ten capacity curves were obtained for each of the sliding, shear, and flexural piers. Tables 3 and 4 list the LHS samples for the shear and sliding piers, respectively.

For the pier failing in flexure, ten values of the Young's modulus, $E$, were determined using LHS sampling: 930, 996, 950, 1097, 835, 1004, 905, 1056, 1038, and 1236. Fig. 11 shows the ten capacity curves of the sliding, shear, and flexural piers for the generated LHS samples. The figure presents a visual representation of the effect of the random pairing of the 10 sets of variable parameters considered for each pier. In all three piers, the various capacity curves obtained from the LHS technique exhibit dispersion in the initial slope (up to 30%) and lateral load capacity (up to 20%). Furthermore, the capacity curves for the sliding pier exhibit significant dispersion (up to 50%) after the onset of sliding (at 3 mm) until collapse. The obtained capacity curves for the three types of URM piers are used as monotonic backbone curves, along with their identified cyclic hysteresis models, in SAP2000 to perform nonlinear time history analyses.

**Table 3**
Latin hypercube samples for the pier failing through diagonal shear cracking.

| **Cohesion,** $c$(N/mm$^2$) | **Friction angle,** $\mu$(rad) | **Young's Modulus,** $E$(N/mm$^2$) |
|---|---|---|
| 0.1479 | 0.6720 | 997.7 |
| 0.1548 | 0.6268 | 893.6 |
| 0.1274 | 0.7485 | 1029.1 |
| 0.1392 | 0.5462 | 1145.6 |
| 0.1414 | 0.6502 | 960.42 |
| 0.1349 | 0.6142 | 815.93 |
| 0.1617 | 0.7183 | 1089.24 |
| 0.1464 | 0.6386 | 930.91 |
| 0.1053 | 0.5688 | 1055.03 |
| 0.1296 | 0.6912 | 1011.13 |

### 3.2. Uncertainty in the seismic demand

On January 26, 2001, an earthquake of Mw 7.6 struck the Gujarat region of India. It was the largest intra-plate earthquake in India [45], with an intensity of X on the modified Mercalli intensity (MMI) scale [46]. The earthquake damaged over a million structures, and the consequent economic loss was close to US$ 10 billion [47–49]. A large number of URM structures were damaged during this destructive earthquake [50]. There was non-uniform and inconsistent damage in the epicentral region [51]. No strong ground motions were recorded during this earthquake, and only PGA data recorded on structural response recorders (SRRs) from 13 stations are available [52]. For nonlinear time history analyses of URM structures damaged in the 2001 Gujarat earthquake, it is essential to assemble a suite of strong ground motions. Because a historical database of strong ground motions is not available for the region, ground motions can either be obtained by the selection and scaling of natural records from other regions or by generating synthetic ground motions. The modified stochastic finite-fault method [27] has been used previously to generate rock-level strong ground motions for the 2001 Gujarat earthquake [53]. The PGAs of these rock-level strong ground motions were observed to reasonably match the PGA data recorded at the 13 stations. The stochastic finite-fault method requires several additional input parameters. The distance-dependent ground motion duration model, source effects (i.e., magnitude, fault size, slip distribution, and stress drop), and path effects (i.e., geometric spreading function, frequency-dependent quality factor, shear wave velocity, and density) have been previously determined appropriately for the Gujarat region and used in simulations [54]. After the validation of PGAs at the bedrock level, the methodology was extended to various other sites in Gujarat.

**Table 4**
Latin hypercube samples for the pier failing through bed-sliding.

| **Cohesion,** $c$(N/mm$^2$) | **Friction angle,** $\mu$(rad) | **Young's modulus,** $E$(N/mm$^2$) | **Poisson's ratio,** $\nu$ | **Residual friction coefficient**(rad) |
|---|---|---|---|---|
| 0.1497 | 0.6201 | 927.39 | 0.265 | 0.5316 |
| 0.1465 | 0.6619 | 1057.22 | 0.228 | 0.5032 |
| 0.1252 | 0.8546 | 1034.92 | 0.283 | 0.4457 |
| 0.1284 | 0.6987 | 793.19 | 0.273 | 0.5994 |
| 0.1429 | 0.5409 | 985.60 | 0.241 | 0.5781 |
| 0.1336 | 0.6116 | 1165.29 | 0.260 | 0.5466 |
| 0.1370 | 0.5698 | 1004.98 | 0.254 | 0.6221 |
| 0.1522 | 0.6482 | 898.85 | 0.213 | 0.5942 |
| 0.1614 | 0.7243 | 973.40 | 0.247 | 0.5506 |
| 0.1155 | 0.6754 | 1084.61 | 0.233 | 0.5155 |

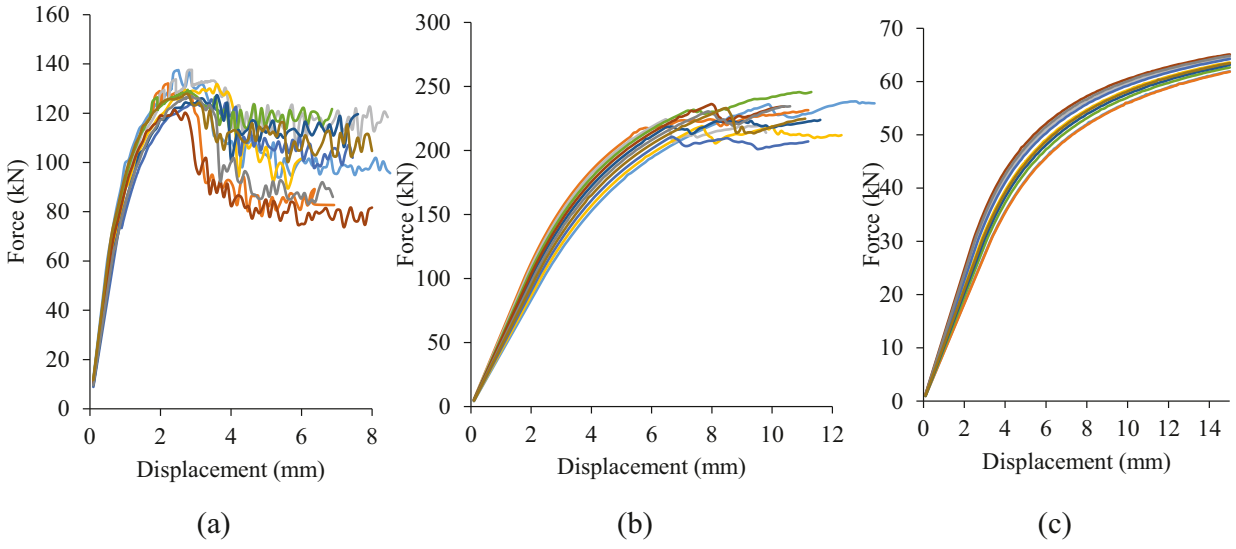


**Fig. 11.** Capacity curves for piers failing through (a) sliding, (b) shear, and (c) flexure (10 LHS samples each).

Further, to obtain surface-level synthetic ground motions for various other sites [54], appropriate soil amplification functions for each site were used [55]. At each site, the ground motions were obtained at the bedrock level and amplified to the surface level.

The consideration of stochastic aspects at the sub-fault level (Gaussian random noise with an underlying spectrum) enables simulations of multiple time histories at each site. In this study, ten random realizations of synthetic ground motions were obtained for each site. In the present study, nonlinear time history analyses (NTHA) were performed using these synthetic surface-level ground motions. Table 5 summarizes the characteristics of these ground motions, such as the PGA, PGV, predominant period ($T_p$), and mean period ($T_m$) along with the mean displacements for the sliding, shear, and flexural piers.

From Table 5, we observe that in towns situated in seismic zone 5 [56], all of the soft-brick URM piers, i.e., the bed-sliding, shear, and flexural piers, reach the collapse limit state. These findings are consistent with damage reconnaissance surveys [46], which stated that most URM structures in these towns suffered "heavy damage," "destruction," and "total damage." The reconnaissance survey [46] assigned an intensity (MMI) of X to Dudhai, Bhachau, and Adesar, and also stated that "most" of the URM structures in the towns of Dudhai, Bhachau, Rapar, and Adesar suffered "total damage." In seismic zone 4, reconnaissance reports stated "heavy damage" to URM structures in the town of Morbi, corroborating the results from the NTHA, which indicate that the sliding, shear, and flexural piers reach the collapse limit state. In the town of Radhanpur, reconnaissance reports stated "heavy damage" to most URM piers; the corresponding results from the NTHA show that the bed-sliding and shear piers reach the collapse limit state, while high displacements approaching the collapse limit state are observed for flexural piers. Other towns in seismic zone 4 [56] had *slight* to *moderate* damage to URM structures, and the findings from the NTHA also indicate that the cracking limit state is reached in all types of piers. For towns in seismic zone 3 [56], the available reconnaissance reports did not quantify the specific level of damage to the existing stock of URM structures, and MMI indices were assigned based on the observed damage in all types of masonry, stone, and reinforced concrete buildings.

URM piers in two towns in seismic zone 3 [56], Rajkot and Surendranagar, exhibited high displacements. Although both towns had records with low PGA, pulse-like features were present in the velocity time histories. Figs. 12, 13, and 14 show the velocity time history from Rajkot and the corresponding pier displacements of the bed-sliding, shear, and flexural piers, respectively. Figs. 15, 16, and 17 show the velocity time history from Surendranagar and the corresponding pier displacements of the bed-sliding, shear, and flexural piers, respectively. The displacement time histories in these cases indicate that the pulse-like features imposed a high strength demand on the piers. Subsequently, there was degradation in the strength and stiffness of the piers, leading to high displacements.

Fig. 18(a,b) show the fragility curves of the sliding, shear, and flexural piers for the cracking and collapse limit states, respectively. The graphs show the probability of exceeding the various limit states of the masonry piers. The PGA represents the seismic intensity. At each PGA level, 100 displacement responses were obtained corresponding to the 100 pier–ground motion pairs used for the NTHA. The probability of exceedance was determined by comparing these responses with the damage state displacement thresholds corresponding to the different failure modes of the piers (identified previously from the numerical modeling of the piers).

**Table 5**
Mean characteristics of synthetic ground motions and NTHA results.

| S. No. | Station | Dist.(km) | MMI | PGA(g) | PGV(m/s) | $T_p$(s) | $T_m$(s) | Disp. Flexural Pier(mm) | Disp.Sliding Pier(mm) | Disp.Shear Pier(mm) |
|---|---|---|---|---|---|---|---|---|---|---|
| Sites in Zone 5 (IS 1893:2016) – PSA(DBE) = 0.45 g | | | | | | | | | | |
| 1 | Dudhai | 15 | X | 0.74 | 0.87 | 0.21 | 0.55 | 14 | 4 | 8 |
| 2 | Bhachau | 19 | X | 0.64 | 0.54 | 0.10 | 0.31 | 14 | 4 | 8 |
| 3 | Suvai | 34 | IX | 0.38 | 0.32 | 0.22 | 0.35 | 14 | 4 | 8 |
| 4 | Lakadia | 36 | IX | 0.42 | 0.53 | 0.18 | 0.50 | 14 | 4 | 8 |
| 5 | Rapar | 46 | IX | 0.33 | 0.18 | 0.11 | 0.19 | 14 | 4 | 8 |
| 6 | Dhori | 49 | X | 0.74 | 0.63 | 0.26 | 0.40 | 14 | 4 | 8 |
| 7 | Khavda | 73 | IX | 0.35 | 0.18 | 0.15 | 0.23 | 14 | 4 | 8 |
| 8 | Bela | 77 | IX | 0.12 | 0.12 | 0.19 | 0.41 | 14 | 4 | 8 |
| 9 | Adesar | 78 | X | 0.15 | 0.13 | 0.19 | 0.38 | 14 | 4 | 8 |
| 10 | Mandvi | 111 | VII | 0.24 | 0.17 | 0.14 | 0.26 | 14 | 4 | 8 |
| 11 | Dayapur | 141 | VIII | 0.13 | 0.09 | 0.16 | 0.29 | 14 | 4 | 8 |
| 12 | Nakhtarana | 155 | VIII | 0.20 | 0.16 | 0.13 | 0.33 | 14 | 4 | 8 |
| 13 | Naliya | 192 | VII | 0.14 | 0.11 | 0.13 | 0.39 | 14 | 4 | 8 |
| Sites in Zone 4 (IS 1893:2016) – PSA(DBE) = 0.30 g | | | | | | | | | | |
| 14 | Dwarka | 183 | VIII | 0.03 | 0.03 | 0.25 | 0.46 | 4.19 | 3.41 | 3.87 |
| 15 | Lalpur | 122 | VIII | 0.09 | 0.05 | 0.11 | 0.18 | 7.09 | 4 | 6.25 |
| 16 | Morbi | 93 | VIII | 0.16 | 0.12 | 0.17 | 0.25 | 14 | 4 | 8 |
| 17 | Radhanpur | 148 | VIII | 0.06 | 0.07 | 0.30 | 0.49 | 10.85 | 4 | 8 |
| 18 | Sipu | 235 | VIII | 0.02 | 0.01 | 0.10 | 0.25 | 1.99 | 1.50 | 1.88 |
| Sites in Zone 3 (IS 1893:2016) – PSA(DBE) = 0.20 g | | | | | | | | | | |
| 19 | Amreli | 256 | VII | 0.017 | 0.006 | 0.08 | 0.13 | 0.77 | 0.58 | 0.81 |
| 20 | Gandhinagar | 248 | VI | 0.012 | 0.010 | 0.15 | 0.32 | 1.47 | 1.06 | 1.54 |
| 21 | Jhagadia | 354 | VI | 0.002 | 0.001 | 0.24 | 0.36 | 0.19 | 0.13 | 0.40 |
| 22 | Junagadh | *235* | VII | 0.019 | 0.010 | 0.09 | 0.17 | 1.65 | 1.02 | 1.67 |
| 23 | Kadana | 369 | V | 0.004 | 0.002 | 0.11 | 0.15 | 0.23 | 0.18 | 0.39 |
| 24 | Kevadia | 396 | V | 0.002 | 0.001 | 0.13 | 0.19 | 0.09 | 0.08 | 0.10 |
| 25 | Rajkot | 129 | VII | 0.065 | 0.074 | 0.45 | 0.54 | 9.14 | 4 | 8 |
| 26 | Surendranagar | 158 | VII | 0.047 | 0.041 | 0.21 | 0.36 | 7.22 | 4 | 7.05 |
| 27 | Ukai | 422 | V | 0.002 | 0.001 | 0.07 | 0.15 | 0.11 | 0.08 | 0.17 |
| 28 | Una | 280 | V | 0.009 | 0.005 | 0.17 | 0.24 | 0.64 | 0.62 | 0.64 |
| 29 | Vadodara | 321 | VI | 0.004 | 0.003 | 0.22 | 0.32 | 0.34 | 0.33 | 0.62 |

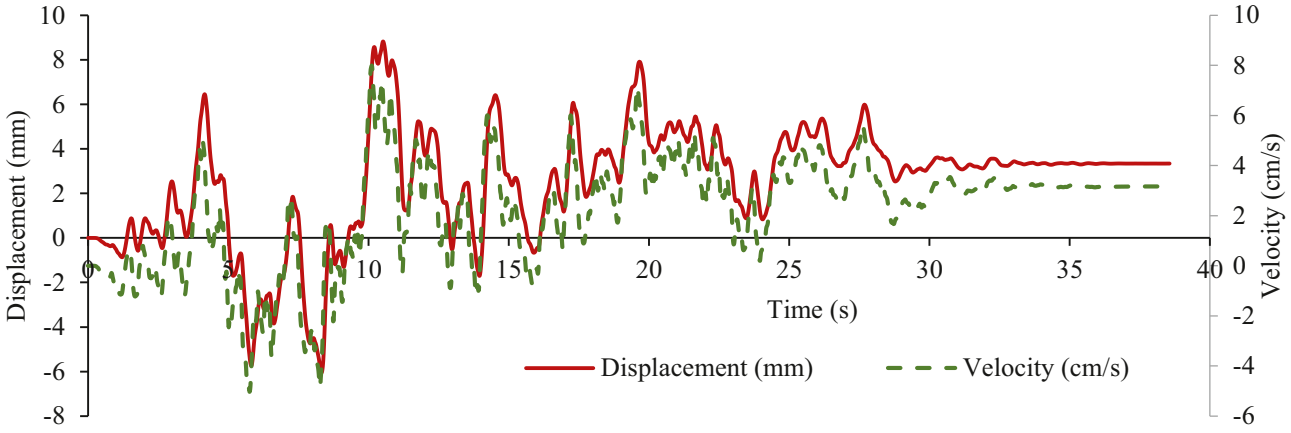


**Fig. 12.** Rajkot velocity time history and pier displacement (Bed-Sliding Pier 1, Ground Motion 1).

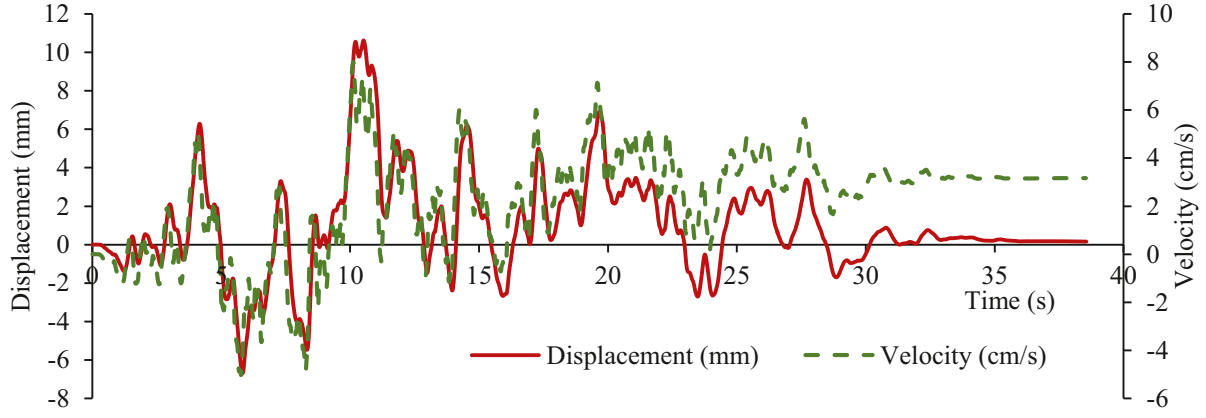


**Fig. 13.** Rajkot velocity pulse time history and pier displacement (Shear Pier 1, Ground Motion 1).

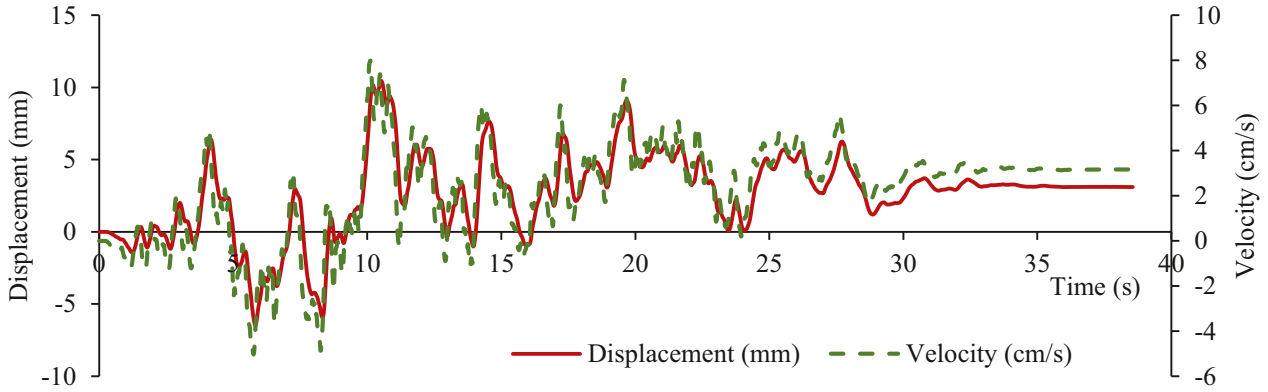


**Fig. 14.** Rajkot velocity time history and pier displacement (Flexural Pier 1, Ground Motion 1).

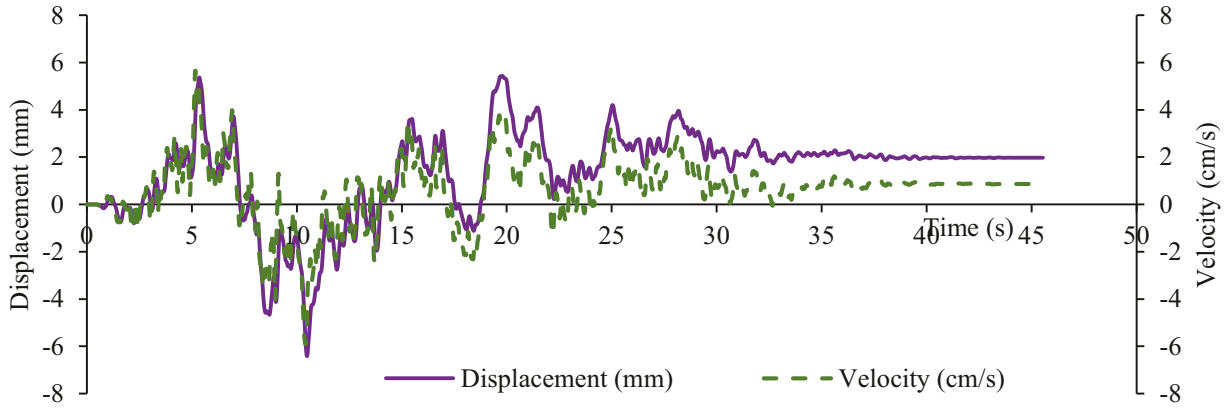


**Fig. 15.** Surendranagar velocity time history and pier displacement (Sliding Pier 1, Ground Motion 1).

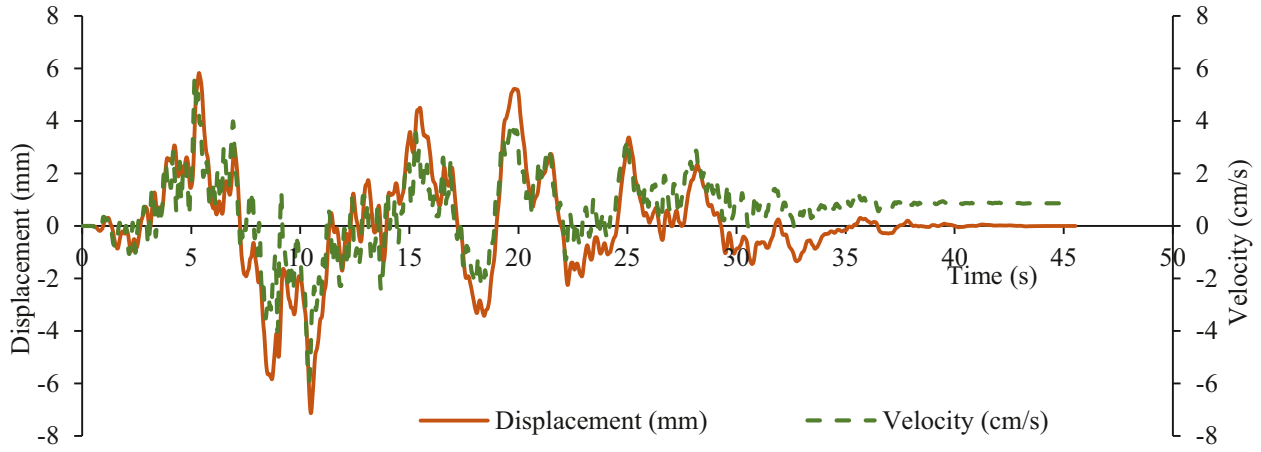


**Fig. 16.** Surendranagar velocity time history and pier displacement (Shear Pier 1, Ground Motion 1).

Fig. 18(a) shows that the bed-sliding, shear, and flexural piers reached the cracking limit state at very low PGA levels of 0.02 g. This ground motion intensity level corresponds to a 50% probability of exceedance of the cracking limit state. According to the Indian seismic code IS1893:2016 [56], the PGA levels for the maximum considered earthquake (MCE) levels corresponding to Zones 5, 4, and 3 are 0.36 g, 0.24 g, and 0.16 g, respectively. The expected seismic hazard across these seismic zones is far greater than the PGA level for the cracking limit state for various pier failure modes. Therefore, soft-brick URM piers would reach the cracking limit state under the expected level of ground motion in all seismic zones of the region.

Fig. 18(b) shows that the bed-sliding piers exceeded the collapse limit state at a PGA level of 0.05 g, and the piers failing in diagonal shear would reach the collapse limit state at a PGA level of 0.07 g. The flexural piers could resist the seismic forces until a comparatively higher PGA level of 0.12 g. These ground motion intensity levels correspond to a 50% probability of collapse. These values are lower than the PGA values provided in IS1893:2016 [56] for the MCE (in all seismic zones) and hence indicate the high level of vulnerability of soft-brick URM piers.

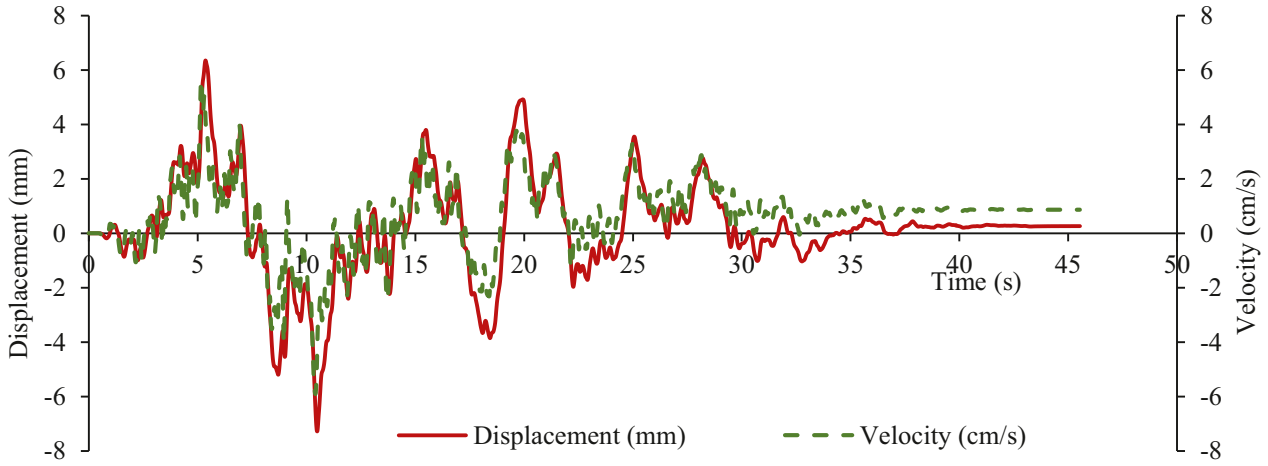


**Fig. 17.** Surendranagar velocity time history and pier displacement (Flexural Pier 1, Ground Motion 1).

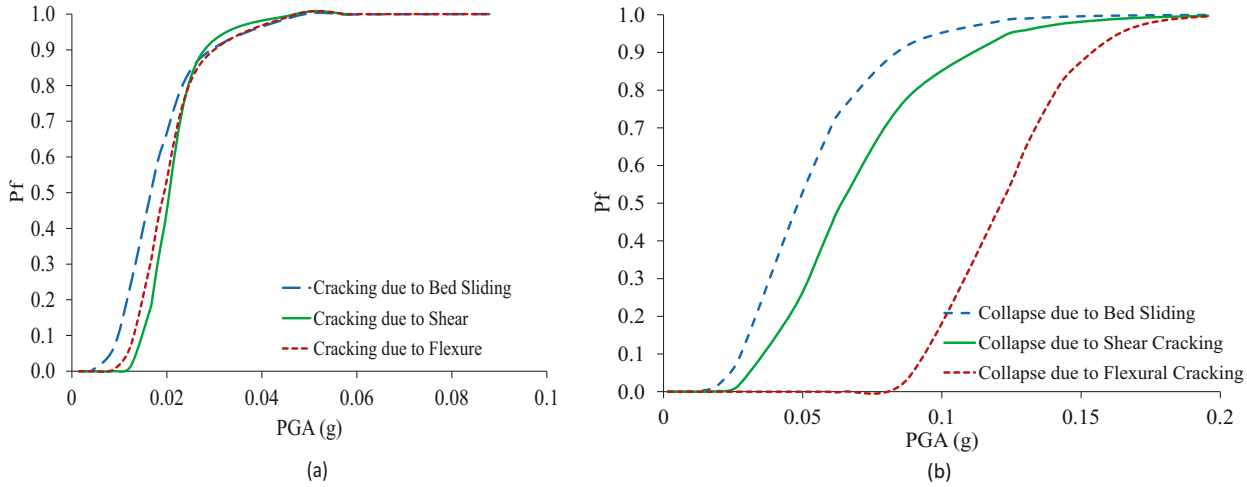


**Fig. 18.** Comparison of the (a) cracking fragility and (b) collapse fragility of bed sliding, shear, and flexural piers.

## 4. Discussion

The NTHA results correlate well with the available damage survey reports [46,57], which describe the destruction of URM structures in seismic zone 5, particularly in the epicentral region. The NTHA results for towns situated in seismic zones 3 and 4 show that the displacement limit states vary from *no damage* to *cracking* and *collapse*. This is in good agreement with the post-earthquake field observations [46,57], which reported damage to URM structures in seismic zones 3 and 4 ranging from *no damage* and *cracking* in seismic zone 3 to *cracking* and *collapse* in seismic zone 4. It is pertinent to observe that the PGA levels for the design basis earthquake (DBE) for seismic zones 3, 4, and 5 in IS1893:2016 [56] are 0.08 g, 0.12 g, and 0.18 g, respectively. The PGA levels corresponding to collapse obtained from the fragility curves for the three masonry pier failure modes (i.e., sliding, shear, and flexure) are much lower than the code-prescribed PGA levels. Soft-brick URM piers will not survive the expected level of ground motion in low seismic zone 3, which has the least seismic hazard among the three zones. Overall, these observations indicate the extremely high vulnerability of soft-brick URM piers under the expected levels of seismic hazard in the Gujarat region.

For a given set of ground motions at a particular PGA level, the variation in pier displacement is primarily due to the inherent stochastic nature of each ground motion, i.e., the variation in the amplitude, phase, frequency content, and duration of the ground motion with time [58,59]. From Table 5, it can be observed that the values of the predominant period, $T_p$, for ground motions at various sites are typically low, ranging from 0.10 to 0.45 s. The natural periods of low-rise URM structures lie within the observed range of predominant periods. However, a poor correlation is observed between pier displacements and single-parameter frequency estimates such as $T_p$ and $T_m$; consequently, frequency parameters are not used to directly represent seismic intensity in the fragility curves. Further, because the seismic hazard levels in IS1893:2016 for various regions of Gujarat are prescribed in terms of the PGA, PGA is used in the present study to represent the seismic intensity in the fragility curves.

Fig. 19 shows the coefficient of variation (CoV) of the displacements of the soft-brick URM piers versus the PGA for the piers failing through flexure, shear, and bed-sliding. The figures illustrate the effect of the uncertainty in the ground motion on three simulated cases for each type of pier. For illustration, the figures show the CoVs of the first, fifth, and tenth iterations of the simulated pier sets. Similarly, the CoVs of the first and second iterations of the simulated ground motion suite are shown in these figures. The CoV for the uncertainty due to ground motions varies from 0.12 to 0.28 for flexural piers, whereas it varies from 0.16 to 0.28 for shear and bed-sliding piers. It is observed that the influence of material uncertainty on seismic fragility is minimal compared to the uncertainty in the ground motion. To compute the CoV due to the ground motion uncertainty, the mean and standard deviation of the pier displacements are calculated for each pier in each failure mode, i.e., flexure, shear, or sliding, under 10 ground motions at each PGA level. Similarly, to compute the CoV due to capacity uncertainty, the

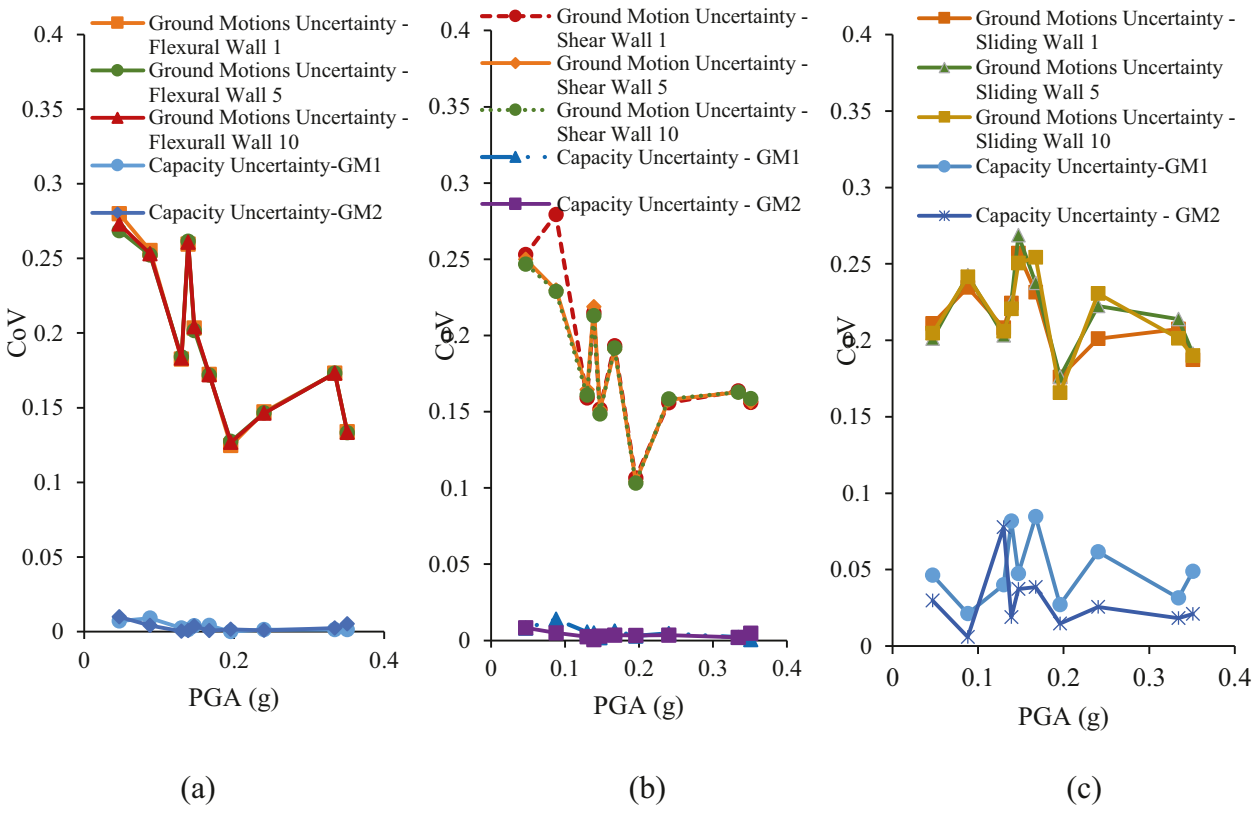


**Fig. 19.** Comparison of the CoVs for ground motion uncertainty and capacity uncertainty in (a) flexural piers; (b) shear piers; and (c) sliding piers.

mean and standard deviation of pier displacements are calculated for each ground motion at each PGA level for all 10 iterations of the pier failing in flexure, diagonal shear cracking, or bed-sliding.

Fig. 19 shows that the structural responses in flexural, shear, and bed-sliding piers are strongly affected by the variability in the suite of ground motions, as compared to the far lesser effect of the material variability. Hence, the selection of ground motion suite is critical, as the ground motions affect the developed seismic fragility curves. Further, it should be noted that in this study, a maximum 20% variation in material properties was assumed. However, owing to an absolute lack of enforcement of quality control in building construction, a much larger variation in material properties can be expected in practice. Damage reconnaissance surveys [42,57] conducted in the aftermath of the 2001 Gujarat earthquake reported the destruction of URM structures in seismic zone 5, as predicted by the seismic fragility curves obtained in this study. In seismic zones 3 and 4, the reconnaissance surveys reported that the observed damage to URM structures varied from cracking to total collapse; these observations also agree well with the findings of the present study. The detailed seismic fragility assessment of URM structures indicates an immediate need for retrofitting using various techniques, such as ferrocement overlays [60], GFRP strips [61], fiber-reinforced cementitious composites [62], steel mesh reinforced shotcrete [63], or steel fiber reinforced mortar coatings [64].

## 5. Conclusion

URM structures constitute a large portion of the building stock in India. A typical URM building comprises piers with various aspect ratios that are subjected to a variety of axial stresses. This study investigates the performance of load-bearing soft-brick URM piers using NTHA. In the absence of experimental results on load-bearing soft-brick URM piers, numerical modeling of piers with various aspect ratios and axial stresses is performed. The parameters required in the constitutive models are obtained from material tests and used to develop a calibrated numerical model of the URM piers. The monotonic and cyclic behaviors are examined to identify the critical displacement limit states. It is concluded that load-bearing piers exhibit distinct changes in failure modes with increases in the level of axial stress and the aspect ratio. Based on the observed cyclic behavior, the isotropic hysteresis model, multi-linear pivot model, and kinematic model are adopted for sliding, shear, and flexural piers, respectively.

Surface-level synthetic ground motions from the Mw 7.6 2001 Gujarat earthquake are used to perform NTHA of the piers. The earthquake caused massive damage to soft-brick URM structures in Gujarat, India. The ground motions from this destructive earthquake are analyzed, and their key characteristics are tabulated. In many towns, the ground motions exhibited low predominant periods, thereby damaging piers with similarly low natural periods. The results of the NTHA performed on the calibrated hysteretic models and the resulting fragility curves indicate that soft-brick bed-sliding piers are highly vulnerable to collapse under ground motions with extremely low PGA values (0.05 g). Soft-brick piers failing through diagonal shear cracking are slightly less fragile and can resist seismic forces up to a PGA level of 0.07 g before collapse. Soft-brick flexural piers can resist collapse up to a PGA level of 0.12 g. Overall, the results indicate that soft-brick URM piers failing in any of the three failure modes are highly vulnerable as their collapse PGA values are lower than the expected seismic intensity in the region. These results also correlate well with damage reconnaissance surveys performed in the aftermath of the earthquake. Further, it can be concluded that URM structures with low-strength soft-brick piers are highly vulnerable to the range of anticipated ground motions in Gujarat.

It is also observed that the uncertainty due to the variation in the capacity of the URM piers is less significant than the uncertainty due to the effect of the variation in strong ground motions. Hence, ground motion suites must be selected meticulously because they have a considerable influence on the results of the nonlinear dynamic analysis. Overall, the fragility curves derived in this study provide an enhanced understanding of the seismic vulnerability of soft-brick URM piers, and the developed

fragility framework can be extended to the complete range of soft-brick URM structures.

## Declaration of Competing Interest

The authors declare that they have no known competing financial interests or personal relationships that could have appeared to influence the work reported in this paper.

## References


[1] PAGER Database. (2007). http://pubs.usgs.gov/of/2008/1160/downloads/OF08-1160.pdf

[2] A. Naseer, A. Naeem, Z. Hussain, Q. Ali, Observed seismic behavior of buildings in northern Pakistan during the 2005 Kashmir earthquake, Earthq. Spectra 26 (2) (2010) 425–449, doi:10.1193/1.3383119.

[3] M.B. Ravula, K.V. Subramaniam, Experimental investigation of compressive failure in masonry brick assemblages made with soft brick, Mater. Struct. 50 (1) (2017) 19.

[4] Bureau of Indian StandardsHandbook on Masonry Design and Construction: SP20, Bureau of Indian Standards, New Delhi, India, 1991.

[5] P. Dayaratnam, Brick and Reinforced Brick Structures, Oxford and IBH, New Delhi, 1987.

[6] G. Sarangapani, B.V. Venkatarama Reddy, K.S Jagadish, Structural characteristics of bricks, mortar and masonry, J. Struct. Eng. 29 (2) (2002) 101–107 (India).

[7] D.P. Abrams, Performance-based engineering concepts for unreinforced masonry building structures, Prog. Struct. Mater. Eng. 3 (2001) 48–56.

[8] W.S. McNary, D.P. Abrams, Mechanics of masonry in compression, J. Struct. Eng. 111 (4) (1985) 857–870.

[9] Atkinson R.H., Noland J.L. (1983). A proposed failure theory for brick masonry in compression. Proceeding of the 3rd Canadian Masonry Symposium, Edmonton, pp 5.1–5.17 5.

[10] R.G. Drysdale, A.A. Hamid, L.R. Baker, Masonry structures: Behaviour and Design, Prentice-Hall, Englewood Cliffs, 1994.

[11] G. Magenes, G.M. Calvi, In-plane seismic response of brick masonry walls, Earthq. Eng. Struct. Dyn. 26 (11) (1997) 1091–1112.

[12] A. Anthoine, G. Magonette, G. Magenes, Shear-compression testing and analysis of brick masonry walls, in: Proceedings of the 10th European Conference on Earthquake Engineering, 3, 1995, pp. 1657–1662.

[13] T. Manzouri, P.B. Shing, B. Amadei, M. Schuller, R. Atkinson, Repair and Retrofit of Unreinforced Masonry Walls: Experimental Evaluation and Finite Element Analysis, Department of Civil, Environmental and Architectural Engineering, University of Colorado, Boulder, Colorado, 1995 Report CU/SR-95/2.

[14] D.P. Abrams, N. Shah, Cyclic Load Testing of Unreinforced Masonry Walls, College of Engineering, University of Illinois at Urbana, 1992 Advanced Construction Technology Center Report #92-26-10.

[15] G.S. Epperson, D.P. Abrams, Evaluating lateral strength of existing unreinforced brick masonry piers in the laboratory, J. Mason. Soc. 10 (2) (1992) 86–93 Boulder, Colorado.

[16] T. Choudhury, H.B. Kaushik, Influence of individual wall strengths on lateral strength of URM buildings constructed using low-strength masonry, J. Earthq. Eng. (2020) 1–28.

[17] M.B. Ravula, K.V. Subramaniam, Cohesive-frictional interface fracture behavior in soft-brick masonry: experimental investigation and theoretical development, Mater. Struct. 52 (2) (2019) 34.

[18] M.B. Ravula, K.V. Subramaniam, Experimental investigation and interface material model for the cohesive–frictional shear response of soft-brick masonry under applied compression, J. Mater. Civ. Eng. 31 (12) (2019) 04019311.

[19] J. Miyakoshi, Y. Hayashi, K. Tamura, N. Fukuwa, Damage ratio functions of buildings using damage data of the 1995 Hyogo-Ken Nanbu earthquake, in: Proceedings of the 7th International Conference On Structural Safety and Reliability (ICOSSAR), 1997, pp. 349–354.

[20] G. Orsini, A model for buildings' vulnerability assessment using the parameter less scale of seismic intensity (PSI), Earthq. Spectra 15 (3) (1999) 463–483.

[21] M. Shinozuka, M.Q. Feng, J. Lee, T. Naganuma, Statistical analysis of fragility curves, J. Eng. Mech. 126 (12) (2000) 1224.

[22] O.S. Kwon, A.S. Elnashai, The effect of material and ground motion uncertainty on the seismic vulnerability curves of RC structure, Eng. Struct. 28 (2006) 289–303.

[23] K. Bakalis, D. Vamvatsikos, Seismic fragility functions via nonlinear response history analysis, J. Struct. Eng. 144 (10) (2018) 04018181.

[24] A. Tsioulou, Simulated Ground Motions For Seismic Risk Assessment of Structures, University College London(UCL), London, UK, 2018 Doctoral dissertation.

[25] D.M. Boore, Simulation of ground motion using the stochastic method, Pure Appl. Geophys. 160 (3–4) (2003) 635–676.

[26] I.A. Beresnev, G.M. Atkinson, FINSIM–a FORTRAN program for simulating stochastic acceleration time histories from finite faults, Seismol. Res. Lett. 69 (1) (1998) 27–32.

[27] D. Motazedian, G.M. Atkinson, Stochastic finite-fault modeling based on dynamic corner frequency, Bull. Seismol. Soc. Am. 95 (2005) 995–1010.

[28] Guneyisi, Altay, Seismic fragility assessment of effectiveness of viscous dampers in R/C buildings under scenario earthquakes„ Struct. Saf. 30 (2008) 461–480.

[29] K. Goda, Yoshikawa, Incremental dynamic analysis of wood-frame houses in Canada: effects of dominant earthquake scenarios on seismic fragility, Soil Dyn. Earthq. Eng. 48 (2013) 1–14.

[30] A.H. Akhaveissy, C.S. Desai, Unreinforced masonry walls: nonlinear finite element analysis with a unified constitutive model, Arch. Comput. Methods Eng. 18 (2011) 485–502, doi:10.1007/s11831-011-9067-4.

[31] L. La Mendola, M. Accardi, C. Cucchiara, V Licata, Nonlinear FE analysis of out-of–plane behaviour of masonry walls with and without CFRP reinforcement, Constr. Build. Mater. 54 (2014) 190–196.

[32] A. Stavridis, P.B. Shing, Finite-element modeling of nonlinear behavior of masonry-infilled RC frames, J. Struct. Eng. 136 (3) (2010) 285–296.

[33] G. Milani, 3D upper bound limit analysis of multi-leaf masonry walls, Int. J. Mech. Sci. 50 (4) (2008) 817–836.

[34] Abdulla, K.F. , Cunningham, L.S. , & Gillie, M. (2017). Simulating masonry wall behaviour using a simplified micro-model approach. Eng. Struct., 151, 349–365. doi:10.1016/j.engstruct.2017.08.021

[35] A. Aldemir, A Simple Seismic Performance Assessment Technique for Unreinforced Masonry Structures, Middle East Technical University, Turkey, 2010 MS Dissertation.

[36] TNO DIANA BV. (2011). *Diana* User Manual. Release 9.4.4, Delft, Netherlands

[37] P.J.B.B. Lourenco, Computational Strategies for Masonry Structures, Delft University of Technology, Holland, 1996 PhD Dissertation.

[38] P.B. Lourenço, J.G. Rots, Multisurface interface model for analysis of masonry structures, J. Eng. Mech. 123 (7) (1997) 660–668.

[39] J.C. Almeida, P.B. Lourenc¸o, J.A. Barros, Characterization of brick and brick–mortar interface under uniaxial tension, in: Proceedings of 7th International Seminar on Structural Masonry for Developing Countries, CEFET-MG, Belo Horizonte, Brazil, 2002, pp. 67–76. 1997.

[40] Federal Emergency Management Agency(FEMA), Evaluation of Earthquake Damaged Concrete and Masonry Wall Buildings: technical Resource, 307, FEMA, 1998.

[41] Computers and Structures Incorporated. (2012). SAP2000 version 15, software. Berkeley, CA

[42] Y. Pan, A.K. Agrawal, M. Ghosn, Seismic fragility of continuous steel highway bridges in New York State, J. Bridge Eng. 12 (6) (2007) 689–699.

[43] M.A. Hariri-Ardebili, V.E. Saouma, Seismic fragility analysis of concrete dams: a state-of-the-art review, Eng. Struct. 128 (2016) 374–399.

[44] G.D. Wyss, K.H. Jorgensen, A User's Guide to LHS: Sandia's Latin Hypercube Sampling Software, Risk Assessment and Systems Modeling Dept., Sandia National Laboratories, Albuquerque, N.M, 1998.

[45] D. Nagamani, P. Mandal, Estimation of earthquake source parameters in the Kachchh seismic zone, Gujarat, India, using three component S-wave spectra, J. Earth Syst. Sci. 126 (2017) 74.

[46] A. Sinvhal, P.R. Bose, V. Prakash, A. Bose, A.K. Saraf, H. Sinvhal, Isoseismals for the Kutch earthquake of 26th January 2001, J. Earth Syst. Sci. 112 (2003) 375–383.

[47] H.K. Gupta, T. Harinarayana, M. Kousalya, D.C. Mishra, I. Mohan, N. Purnachandra Rao, P.S. Raju, B.K. Rastogi, P.R. Reddy, D. Sarkar, Bhuj earthquake of 26 January 2001, J. Geol. Soc. India 72 (2001) 245–252.

[48] H.K. Gupta, N. Purnachandra Rao, B.K. Rastogi, D. Sarkar, The deadliest intraplate earthquake: perspectives, Science 291 (2001) 2101–2102.

[49] B.K. Rastogi, H.K. Gupta, P. Mandal, H.V.S. Satyanarayana, M. Kousalya, R. Raghavan, R. Jain, A.N.S. Sarma, N. Kumar, C. Satyamurty, The deadliest stable continental region earthquake occurred near Bhuj on 26 January 2001, J. Seismol. 5 (2001) 609–615.

[50] K.S. Jagadish, S. Raghunath, K.N. Rao, Behaviour of masonry structures during the Bhuj earthquake of January 2001, J. Earth Syst. Sci. 112 (3) (2003) 431–440.

[51] J.L. Chatelain, B. Guillier, I.A. Parvez, False site effects: the anjar case, following the 2001 Bhuj (India) earthquake, Seismol. Res. Lett. 79 (2008) 816–819.

[52] C.H. Cramer, A. Kumar, 2001 Bhuj, India, earthquake engineering seismoscope recordings and Eastern North America ground-motion attenuation relations, in: Bull. Seismol. Soc. Am., 93, 2003, pp. 1390–1394.

[53] S. Chopra, D. Kumar, B.K. Rastogi, Estimation of strong ground motions for 2001 Bhuj (Mw 7.6), India Earthquake, Pure Appl. Geophys. 167 (2010) 1317–1330 2010.

[54] J. Vemuri, S. Kolluru, S. Chopra, Surface level synthetic ground motions for M7. 6 2001 Gujarat earthquake, Geosciences 8 (12) (2018) 429 (Basel).

[55] S. Chopra, D. Kumar, B.K. Rastogi, P. Choudhury, Yadav, R.B.S. Estimation of site amplification functions in Gujarat region, India, Nat. Hazards 65 (2013) 1135–1155.

[56] Bureau of Indian StandardsIs 1893 Indian Standard Criteria for Earthquake Resistant Design of Structures: Part 1– General Provisions and Buildings, BIS, New Delhi, India, 2016 2016.

[57] J.P. Narayan, M.L. Sharma, A. Kumar, A seismological report on the 26 January 2001 Bhuj, India earthquake, Seismol. Res. Lett. 73 (3) (2002) 343–355.

[58] K.R. Karim, F. Yamazaki, Effect of earthquake ground motions on fragility curves of highway bridge piers based on numerical simulation, Earthq. Eng. Struct. Dyn. 30 (12) (2001) 1839–1856.

[59] D.H. Kim, S.G. Lee, I.K. Lee, Seismic fragility analysis of 5 MW offshore wind turbine, Renew. Energy 65 (2014) 250–256.

[60] A. Hasnat, R. Ahsan, S.M. Yashin, Quasi-static in-plane behavior of full-scale unreinforced masonry walls retrofitted using ferro-cement overlay, Asian J. Civ. Eng. (2022) 1–16.

[61] E. Ahani, F. Osmanzadeh, M.N. Mousavi, B. Rafezy, In-plane retrofitting of masonry structures by using GFRP strips in the bedjoints, Bull. Earthq. Eng. (2022) 1–30.

[62] S.H. Park, N.H. Dinh, S.H. Kim, J.W. Hwang, H.H. Pham, S.J. Lee, K.K. Choi, Seismic retrofit of unreinforced masonry walls using precast panels of fiber-reinforced cementitious composite, J. Build. Eng. 53 (2022) 104548.

[63] M.E. Moeini, S.A. Razavi, M. Yekrangnia, P. Pourasgari, N. Abbasian, Cyclic performance assessment of damaged unreinforced masonry walls repaired with steel mesh reinforced shotcrete, Eng. Struct. 253 (2022) 113747.

[64] S.S. Lucchini, L. Facconi, F. Minelli, G. Plizzari, Cyclic test on a full-scale unreinforced masonry building repaired with steel fiber-reinforced mortar coating, J. Struct. Eng. 147 (6) (2021) 04021059.